Organic Electronics 128 (2024) 107023

Contents lists available at ScienceDirect

Organic Electronics

journal homepage: www.elsevier.com/locate/orgel

Design of an optical sensor based on organic optoelectronics and nanoplasmonics for multiplex and multimodal detection

Emilia Benvenuti [a], Salvatore Moschetto [a], Marco Angelini [b], Franco Marabelli [c], Marco Natali [a], Paola Pellacani [d], Margherita Bolognesi [a,*], Mario Prosa [a,**], Stefano Toffanin [a,***]

[a] Institute of Nanostructured Materials, National Research Council, Via Piero Gobetti 101, 40129, Bologna, Italy
[b] Optics for Life, Via Roma 67, 27020, Trivolzio, Italy
[c] Department of Physics, University of Pavia, Via Bassi 6, 27100, Pavia, Italy
[d] Plasmore S.r.l, Via Vittorio Emanuele II 4, 27100, Pavia, Italy

ARTICLE INFO

Keywords:
Optical sensors
Organic optoelectronics
System integration
Plasmon enhanced fluorescence
Surface plasmon resonance

ABSTRACT

—On-site analysis of multiple analytes from different classes (such as heavy metals, proteins and small molecules), at the sensitivity required for a selected application, is a hard technological challenge. In this context, optical sensing in miniaturized systems has the largest potential. We present here the design and optimization of a miniaturized optical sensor with multiple channels, capable of multimodal optical detection in each channel, and the proof-of-concept realization of sub-systems providing two complementary detection modes: plasmon enhanced fluorescence and localized surface plasmon resonance. The multichannel (enabling multiplexing) and multimodal optical sensor is designed to have a total size of one inch-square and optimized sensing performance, obtained by combining organic optoelectronic and nanoplasmonic components.

1. Introduction

Optical sensing represents one of the most sensitive and robust methodologies for the detection of analytes of interest in various application scenarios, from food and environmental monitoring to biodiagnostics [1,2]. A larger exploitation on the market of this class of sensors is expected once the technological challenges in miniaturization, portability, and user-friendliness are overcome [3], while fit-for-purpose sensing performances are maintained [4].

Optical sensors are typically divided into different classes depending on their detection mode. Often, a specific detection mode is optimal for a single class of analytes, in a certain range of concentrations, thus for a single specific application field. For example, Surface Plasmon Resonance (SPR) sensing is best suited for label-free detection of high molecular weight analytes (such as proteins) [5]. Differently, optical sensing based on fluorescence is the state-of-the-art detection mode for microbiological targets. In any case, the standard use of both methodologies often requires bulky, costly and delicate benchtop instruments unsuitable for on-site analysis.

Combining in a single miniaturized sensor multiple optical detection modes is a challenging yet innovative approach, which would allow to: i) enlarge by orders of magnitude the dynamic range of detection of a specific analyte (i.e. for Hg^{2+} a detection range of 25 nM-50 μM is expected for SPR, whereas 0.5–50 nM is expected for Fluorescence) [6,7]; ii) provide a built-in control for techniques which are sensitive to different interferences [8]; iii) perform in a single sensor detection of multiple analytes from different classes (i.e. small molecular contaminants, heavy metals, proteins).

Organic optoelectronics is an attractive option for the development of compact and cost-effective sensors due to the possibility to obtain nanometer-thick devices in which the materials in the active layers can be processed by low-temperature processing techniques [9] and be implemented in relevant real settings [10]. Further, their optoelectronic features are easily tunable by a targeted synthesis [11] and design of the organic compounds comprising the device stack [12]. The capability to fabricate miniaturized organic optoelectronic components, such as organic light-emitting diodes (OLEDs) and organic photodiodes (OPDs), with customized shapes promotes their integration, respectively as light

* Corresponding author.
** Corresponding author.
*** Corresponding author.
E-mail addresses: margherita.bolognesi@cnr.it (M. Bolognesi), mario.prosa@cnr.it (M. Prosa), stefano.toffanin@cnr.it (S. Toffanin).

https://doi.org/10.1016/j.orgel.2024.107023
Received 12 October 2023; Received in revised form 22 February 2024; Accepted 28 February 2024
Available online 6 March 2024

sources and light detectors, for the realization of optical sensors [13,14].

In our recent works we developed a miniaturized, highly integrated, and prism-free optical biosensor based on Localized SPR (LSPR) [15,16]. The system integrates organic light sources and light detectors for optical-to-electrical signal transduction, and a nanoplasmonic grating (NPG) functionalized with bioreceptors as the sensing surface. The high level of miniaturization and integration allowed us to obtain seven sensing channels (multiplex format) in a 1-inch square chip. Moreover, we demonstrated that the same NPG developed for LSPR enables also plasmonic enhancement of fluorescence (Plasmon-Enhanced Fluorescence or PEF) [17–19]. In details, the fluorescence from a model fluorophore in proximity of the grating surface, excited and detected at the rear side, was enhanced by 10 times by the plasmonic modes of the NPG.

Based on our previous findings, in this work we report on the design and proof-of-concept demonstration of a new optical sensor capable of performing multimodal detection of model solutions through LSPR and PEF detection modes activated on the same sensing surface. This is enabled by the design of the organic optoelectronic and nanoplasmonic components with specific spectral, optical and geometrical characteristics, and their optimized combination, miniaturization and integration in the same optical sensor. The final optical sensor has a total size of one inch-square and hosts six sensing channels, each one performing dual-mode detection (multimodal). Furthermore, the biofunctionalization of the NPG surface with target-specific bioreceptors would enable the use of the developed sensor in real-setting applications. In this context, a different bio-functionalization on the six different sensing channels would allow the simultaneous analysis of multiple analytes (multiplexing) into the same sensor.

2. Materials and methods

2.1. Simulations

Optical simulations were performed with the optical raytracing software Zemax OpticStudio SW. The method was based on Monte-Carlo ray tracing with 10^8-10^9 rays traced. Random and Sobol algorithms were used for optimal ray tracing distribution and optimization. The light emitted from each OLED was modelled as a true Lambertian emission, with emission spectra following the experimental ones, discretized as histogram bars with 10 nm steps over the 500–1000 nm range, and with a total emission power matching the experimental ones. The spectral response of the OPD was modelled following the experimental spectra, discretized as histogram bars with 10 nm steps over the 500–1000 nm range, and with a total spectral response matching the experimental one. The NPG was modelled as a reflective coating with angle- and wavelength-variable reflectivity, based on the experimental spectral reflectivity at wavelengths in the 500–1000 nm range and at angles in the 0–60° range. The optical filter was modelled as an ideal Long Pass filter with band edge centered at 740 nm. The extinction coefficient, absorption and emission spectra, and quantum yield of the model fluorophore AlexaFluor 750 extrapolated from the datasheet from the commercial provider were introduced in the model, discretized as histogram bars with 10 nm steps in the 500–900 nm range. Fluorophore molecules of Alexa Fluor 750 were modelled as dispersions in a 10 nm thick solid volume onto the sensing surface, at two different densities ($6{\cdot}10^{10}$ and $6{\cdot}10^{12}$ mol/cm^3). All the materials were modelled as true optical materials including Fresnel losses and internal absorption.

2.2. Materials

For the OLEDs and OPDs fabrication, N,N′-di(1-naphthyl)-N,N′-diphenyl-(1,1′-biphenyl)-4,4′-diamine (NPD), Tris(8-hydroxy-quinolinato) aluminium (Alq_3), Platinum octaethylporphyrin (Pt(OEP)), molibdenum oxide and fullerene (C_{60}) were purchased from Sigma Aldrich; Zinc (II) phthalocyanine (ZnPc) was purchased from TCI Europe; Dipyrazino[2,3-f:2′,3′-h]quinoxaline-2,3,6,7,10,11-hexacarbonitrile (HAT-CN), 2,2′,2-(1,3,5-benzinetriyl)-tris(1-phenyl-1-H-benzimidazole) (TPBi) and Platium(II) 5,10,15,20-tetraphenyltetrabenzoporphyrin (Pt(tpbp)) were purchased from Luminescence Technology Corp. Rhodamine 700 (LD700) used for the fluorescence tests was purchased from Exciton. All chemicals were used as received without further purification.

2.3. Device fabrication

The sensors were fabricated on 25 × 25 mm (1 inch-square) glass substrate. First, glass substrates were cleaned by sonication in acetone for 10 min, then in 2-propanol for 10 min. The OLED and OPD stacks were deposited via thermal evaporation through fine metal masks in a high-vacuum deposition chamber at a base pressure of 10^{-8} mbar.

In particular, top-adsorbing OPDs were fabricated directly onto glass substrate according to the following stack: glass/Ca (thickness: 3 nm)/Ag (thickness: 100 nm)/HAT-CN (thickness: 45 nm)/ZnPc:C_{60} (mixing ratio: 50:50; total thickness: 60 nm)/C_{60} (thickness: 30 nm)/TPBi (thickness: 6 nm)/Ca (thickness: 3 nm)/Ag (thickness: 15 nm)/Alq_3 (thickness: 120 nm).

Then a 900 nm thin film of a transparent fluoropolymer (Cytop, from AGC Chemicals Europe Ltd) was deposited as insulating layer by spin coating on top of the OPDs. To remove the residual solvent from the polymeric layer, an annealing step of 2 h at 80 °C was carried out in a vacuum oven.

Top-emitting OLEDs were fabricated on top of the Cytop layer by thermal deposition in high-vacuum. The structure of the top-emitting OLEDs dedicated to the LSPR detection presents the following structure: Ca (thickness: 3 nm)/Ag (thickness: 100 nm)/MoOx (thickness: 60 nm)/NPD (thickness: 30 nm)/Alq_3:Pt(tpbp) (doping 6%; total thickness: 30 nm)/TPBi (thickness: 25 nm)/Ca (thickness: 3 nm)/Ag (thickness: 15 nm)/NPD (thickness: 60 nm).

The structure of the top-emitting OLEDs dedicated to the fluorescence detection presents the following structure: Ca (thickness: 3 nm)/Ag (thickness: 100 nm)/MoOx (thickness: 40 nm)/NPD (thickness: 30 nm)/Alq_3:Pt(OEP) (doping 10%; total thickness: 30 nm)/TPBi (thickness: 25 nm)/Ca (thickness: 3 nm)/Ag (thickness: 15 nm)/NPD (thickness: 60 nm).

The complete system was encapsulated with a glass lid attached to the substrate with a UV-cured glue. In the case of the system dedicated to LSPR, a glass lid decorated with a NPG on top of the outer surface was used.

2.4. NPG fabrication

The fabrication and characterization of the developed nanostructured surface have been described in details in Refs. [15,16].

2.5. Optoelectronic characterization

The OPD current density-voltage curves in the dark and under illumination were recorded inside a glovebox by a Keithley 236 source-measure unit and using a simulated AM1.5 G illumination of 100 mW/cm^2 (Abet Technologies Sun 2000 Solar Simulator). The External Quantum Efficiency (EQE) spectra of the OPDs were measured in air by using a home-made setup and encapsulated devices. Light from a Xe arc lamp (300 Watt of total optical power), coupled with a monochromator (from Spectra-Pro) to produce monochromatic light with steps of 2 nm, was pulsed by means of an optical chopper (Thorlabs) at 80 Hz and was used to illuminate a single OPD. The photocurrent generated from the OPD, driven at 0 V, was collected by a digital lock-in amplifier (Stanford Research Systems SR830). A calibrated Silicon photodiode was used as the reference.

OLED characterization was performed in a glovebox using a standard SUSS probe station coupled to a B1500A Agilent semiconductor device analyzer. The total optical power emitted by the OLED from the top was

measured through a calibrated silicon photodiode (sensitivity of 0.49 A W^{-1} at 766 nm). Electroluminescence spectra on encapsulated OLEDs were collected in air by using a calibrated optical multichannel analyzer (PMA-11, Hamamatsu).

In the case of the LSPR-dedicated optical sensor, the OLED was biased at a fixed current density of 31 mA/cm^2 during the measurement, while the photocurrent of the OPDs was recorded by an Electrochemical Workstation (Autolab, PGSTAT128 N + ECD module). The photocurrent was collected over time when the NPG surface was alternately and sequentially exposed to ethanol/water solutions at different concentrations by injections in the fluidic cell (reaction chamber chip, volume 50 µl by Microfluidic ChipShop). Ethanol/water solutions with 50%, 25%, 10% and 2% v/v concentrations were used.

The optical sensor for the fluorescence detection was tested with a benchmark fluorophore solution of Rhodamine 700 (LD700) in ethanol. Solution at a concentration of $1{\cdot}10^{-4}$ M, $1{\cdot}10^{-5}$ M and pure ethanol were tested by placing the solution in a quartz cuvette (Macro cell type 110-QS Hellma Analytics, volume 350 µl, optical path 1 mm) in direct contact with the encapsulation cap surface of the sensor. The OPD photocurrent was collected through a B1500A Agilent semiconductor device analyzer when OLEDs were driven at a constant current density of 31 mA/cm^2.

3. Results and discussion

3.1. Optical sensor design

In the concept of the proposed multimodal optical sensor, each single channel comprises three different organic optoelectronic components: two organic light emitting diodes (OLEDs) and an optically selective organic photodiode (OPD) (Fig. 1). These components are integrated underneath the sensing surface, which is the NPG. The two detection modes, LSPR and PEF, are independently enabled by optical excitation from the two different OLEDs which can illuminate the NPG surface in a back-reflection configuration. Both optical signals of LSPR and PEF modes are collected by the OPD which converts them into an electrical output signal. In the LSPR detection mode, the light emitted by the OLED for LSPR impinges the portion of the NPG above that OLED. In presence of an analyte attached/in proximity of that portion of the NPG surface, a local change of the refractive index occurs, the spectral reflectivity of the NPG changes accordingly, and the fraction of back-reflected light reaching the OPD changes (with respect to the reference signal collected by the OPD in absence of analytes). The light-intensity change is transformed by the OPD in a photocurrent change (ΔI) over a base photocurrent (I_0). The final LSPR signal is calculated as $\Delta I/I_0$.

In the PEF detection mode, the light emitted by the OLED for PEF impinges the portion of the NPG surface above that OLED and, if no fluorophores are present on the surface, light is partially backscattered towards the OPD. This backscattered fraction of OLED light can be reduced by the insertion of an ad-hoc developed filter. In presence of fluorophores attached/in proximity of the NPG surface, a fluorescence signal from the fluorophore, enhanced by the NPG, is produced and detected by the OPD. Also in this case, the light-intensity change due to the presence of the fluorophore is transformed by the OPD in a photocurrent change. The final PEF signal is calculated as a photocurrent variation in presence and in absence of the fluorophore (ΔI) divided by the base photocurrent (I_0) produced in absence of the fluorophore.

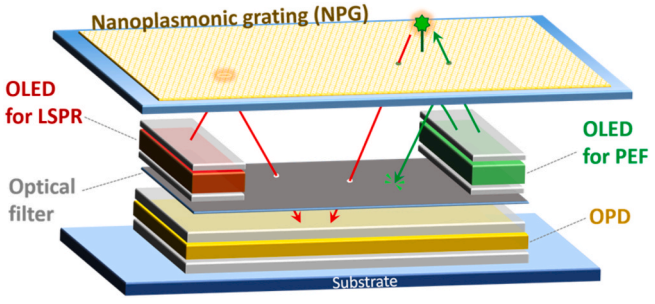

Fig. 1. Schematics of the optical sensor concept with indication of the organic optoelectronic and nanoplasmonic components enabling both LSPR and PEF detection modes.

To design the sensor, first the spectral requirements of all optoelectronic and plasmonic components must match one with each other. For LSPR the best spectrally matched components (OLED for LSPR, NPG and OPD) were already individuated in our previous work [16]. For PEF, spectral matching of the components should consider the maximum of the electroluminescence spectrum of the OLED for PEF, the spectral absorption and emission of the fluorophore, the maximum of the spectral sensitivity of the NPG in terms of plasmonic enhancement, and the spectral response of the OPD. To improve the fluorescence signal-to-noise ratio and avoid the absorption by the OPD of the back-scattered excitation light, a band- or long-pass optical filter should be integrated to produce an optically selective OPD. The optical filter must have a low transmittance in the spectral region of the electroluminescence of the OLED for PEF and a high transmittance in the spectral region of the fluorophore emission (and in that of the electroluminescence of the OLED for LSPR). The model fluorophore Alexa Fluor 750 was considered the best candidate for the optical sensor design, due to its good spectral matching with both NPG and OPD spectral features. Indeed, conjugates of Alexa Fluor 750 on primary and secondary antibodies are widely used in biosensing technologies [20]. Two possible OLEDs for PEF are selected to match with the selected optoelectronic and plasmonic components and fluorophore: one based on the emitter Tris(1-phenylisoquinoline)iridium(III), $Ir(piq)_3$, and one based on the emitter Platinum(II)2,3,7,8,12,13,17,18-octaethyl-21H,23H-porphyrin, Pt(OEP) [21,22]. These two OLEDs for PEF are selected respectively for the high quantum yield of emission ($Ir(piq)_3$), and for the narrow emission spectrum (Pt(OEP)) that minimizes the spectral overlap with the fluorophore emission band.

Once having selected the optoelectronic and plasmonic components that best respond to the spectral requirements, the design of the miniaturized, multichannel and multimodal optical sensor should also consider geometrical requirements. The geometrical design should balance two factors: first, enabling a substantial number of operational channels on the same substrate allowing the detection of multiple analytes in a single sensor (once a suitable multiple biofunctionalized stripes are deposited on the NPG surface); second, maximizing the active surface areas of the OPDs and OLEDs to maximize the collected photocurrent signal. Finally, to allow the experimental realization of the multiple organic optoelectronic components of the optical sensor onto the same substrate, the lateral separation between adjacent OLEDs and OPDs must fulfill fabrication tolerances (i.e. by thermal sublimation in high vacuum and patterning through fine metal masks) and electrical insulation and optical transparency should be guaranteed between vertically stacked components (i.e. monolithically integrated OLEDs and OPDs).

Considering that devices are non-ideal 3D elements, as for instance the OLED is not a point-like emitter, the optimal design of the optical sensor must take into consideration the multiple-wavelengths and multiple-angles contributing to the final LSPR and PEF signals and optimize them both in terms of signal change (%) with respect to reference signal and as absolute values. Optical simulations by the optical software Zemax OpticStudio SW were carried out to optimize both the LSPR and PEF signals, and the layout of the complete system. All the spectral and optical characteristics of the organic optoelectronic and plasmonic components selected above were included in the simulation.

It has been demonstrated [15,18], than a quasi-normal incidence (excitation/collection within a solid angle of 15°) is the optimal geometrical condition for the operation of the NPG, thus ensuring both the highest LSPR and PEF signals. However, pure fluorescence emission

is isotropic over a 360° solid angle and can add a significant contribution to the total signal from a fluorescent target, in addition to the PEF signal. As a compromise, for the simulations the starting layout of a single channel of the multimodal optical sensor is reported in Fig. 2a and comprises: i) three side-by-side top-emitting OLEDs, fabricated in a vertical stack on a top-absorbing OPD, ii) an optical spacer/filter between the OLEDs and the OPD; iii) in the OLEDs plane, one OLED for LSPR is central, and two OLEDs for PEF are at the two sides. To note, since the OLED emission is Lambertian, a relevant number of photons will not contribute to the excitation of the fluorescence signal since they do not impinge a useful portion of the NPG surface. Thus, two OLEDs lateral to the useful portion of the NPG are used for maximizing the excitation of fluorescence.

As a first output from the implementation of the simulation tool, we estimated the collected photocurrent signal in the case of LSPR modality and we use this result to compare the here-reported configuration for LSPR detection (vertical stack configuration) with the one we reported in Ref. [16] (side-by-side configuration) and that we demonstrated to work in real-setting conditions (side-by-side configuration). In particular, we used the same values adopted in the already demonstrated side-by-side configuration (see Fig. S1) for: i) the lateral dimension of the OLED for LSPR and ii) the lateral dimension of the light-sensing surface of the OPD. These dimensions were implemented into the here-designed configuration (see Fig. S2 and Fig. 2a) and the effect on the LSPR signal of the two different configurations was therefore evaluated.

Fig. 2b reports an example of the distribution of the irradiance impinging on the sensing area of the OPD in the two configurations, as resulting from simulations. The light signals impinging on the OPD, before and after the change of refractive index at the NPG surface, are converted into photocurrent signals. The LSPR signal is calculated as the ratio between the variation of the OPD photocurrent (ΔI) over the OPD base photocurrent (I_0) due to a change of the refractive index (Δn) in the medium at the NPG surface of about 10^{-3} Refractive Index Units (RIU) starting from a refractive index of 1.333 (water as the standard). Such Δn roughly corresponds to the refractive index change given on the sensing surface by a 50 μg/ml solution of proteins, as reported in Ref. [16], thus it is a meaningful value for simulating a biological assay condition.

The resulting simulated LSPR signals ($\Delta I/I_0$) for the two configurations are reported in Table 1, together with the base photocurrent I_0 and the photocurrent signal variation ΔI.

For the reference side-by-side configuration, the simulated LSPR signal $\Delta I/I_0$ of 0,07 % over a base photocurrent I_0 of $1.8{\cdot}10^{-7}$ A is in perfect agreement with the experimental results from our previous work [16], confirming the validity of the simulation tool and implemented models. If comparing the side-by-side configuration (already assessed in a complete sensor system prototype) with the more compact vertical stack layout here proposed, the absolute value of ΔI is almost the same while a slightly higher I_0 is responsible for a small reduction of LSPR signal ($\Delta I/I_0$ = 0,04 %) as compared to the side-by-side layout ($\Delta I/I_0$ = 0,07 %). Nevertheless, this small decrease of performance is offset by a significant improvement in terms of compactness and implementation of dual-modality sensing. In addition to that, the expected absolute values of ΔI in the here designed vertical-stack configuration are comparable to values previously collected by portable electronic circuitry [16].

As a further step forward in the optimization of the optical sensor, we also simulate the influence on the LSPR signal of the vertical distance between the NPG and the OLED for LSPR, and of the vertical distance between the OLED for LSPR and the OPD (z_1 and z_2 in Fig. 2a, respectively). The simulations indicate that for heights of z_1 of 0.7, 1.0 or 1.2 mm, the largest z_1 gives the best LSPR signal ($\Delta I/I_0$ of 0.04%), against a $\Delta I/I_0$ of 0.02% and 0.03% for z_1 = 0.7 mm and 1.0 mm respectively. This confirms that, by restricting the range of the solid angles of the light-excitation/light-collection, the overall LSPR signal increases.

Table 1
Comparison between the LSPR signals in reference and proposed configurations.

Configuration	LSPR signals		
	I_0 (A)	ΔI (A)	$\Delta I/I_0$ (%)
Side-by-side (reference)	$1.8{\cdot}10^{-7}$	$1.3{\cdot}10^{-10}$	0,07 %
Vertical stack (proposed in this work)	$3.6{\cdot}10^{-7}$	$1.4{\cdot}10^{-10}$	0,04 %

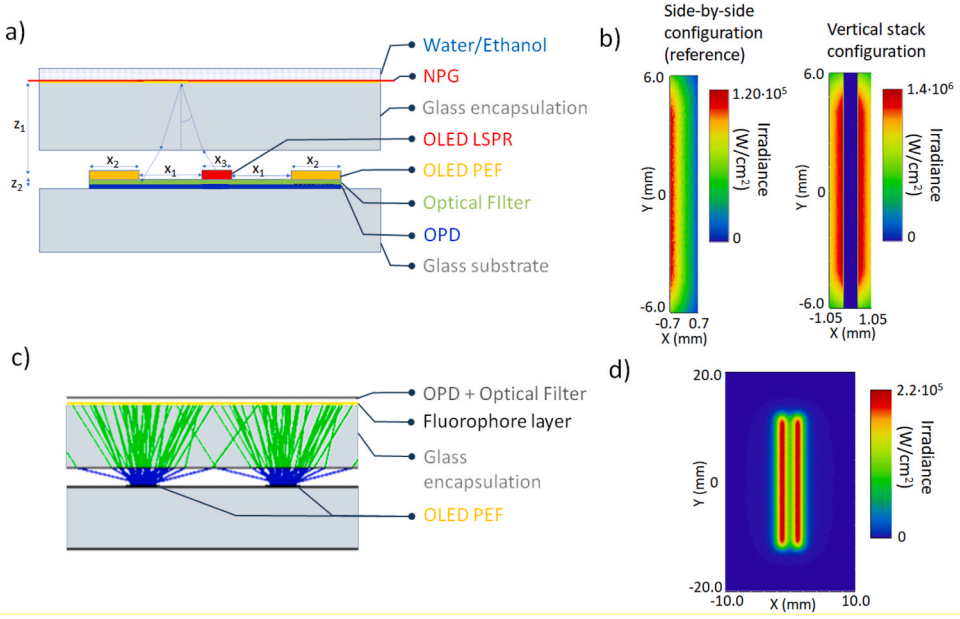

Fig. 2. a) Side view of a single channel of the vertical stack configuration used for the simulations of the LSPR signal. $x_1{+}x_1$ = 1.40 mm is the lateral dimension of the light-sensing surface of the OPD; x_2 = 0.5 mm is the lateral dimension of the OLEDs for PEF; x_3 = 0.5 mm is the lateral dimension of the OLED for LSPR b) Distribution of the incoherent irradiance intensity on the OPD in the side-by-side (left) and vertical stack (right) configurations for LSPR. Side (c) and top (d) views of the layout of a single channel of the system, used for simulating the fluorescence signal, comprising two OLEDs based on Pt(OEP) emitter for PEF, the encapsulation glass, the fluorescence layer, the spectrally selective OPD (OPD + ideal optical filter).

Moreover, a change in z_2 from 3 μm up to 300 μm does not affect the LSPR signal, releasing some geometrical constrain on the integration of the optical filter and/or spacer layer.

For the simulation and optimization of the PEF signal, it was not possible to introduce in Zemax OpticStudio SW the model of the NPG. Indeed, the number of experimental results on the PEF signals from the fluorophore/NPG system [18,19], in particular at variable angles, resulted too low for the creation of a fully reliable model in Zemax. For this reason, here two simplifications are done: i) a pure fluorescence signal (instead of PEF signal) is estimated, with enhancements effects from the NPG taken into account in a second step as a multiplicative factor (·10, following our precedent results) [18,19]; ii) the fluorescence signal is collected at the front side of the NPG (Fig. 2c) and evaluated by placing in that position the OPD covered by an ideal optical filter, i.e. with transmittance 100% above 740 nm and 0% below 740 nm. This is done to exclude the NPG effects which cannot be modelled. The simulation also considers a 10 nm thick layer of fluorophore molecules (Alexa Fluor 750) dispersed in a solid volume: this configuration may mimic the surface functionalization of fluorophores onto NPG surface as expected in the case of PEF [19]. The fluorescence signal is simulated by considering: i) two different densities of the fluorophore ($6{\cdot}10^{10}$ and $6{\cdot}10^{12}$ mol/cm^3); ii) two different OLEDs for PEF (reported above).

Table 2 reports the estimated photocurrent signals, pure fluorescence and PEF signals, for all cases, as follows: I_0, that is the OPD photocurrent generated by the undesired OLED light passing through the optical filter; I_F, that is the OPD photocurrent only due to the fluorescence emitted by the fluorophore molecules, once the undesired OLED light is subtracted; the pure fluorescence signal, calculated as I_F/I_0 (%); the PEF signal, calculated as the pure fluorescence signal multiplied by 10 times.

The largest fluorescence signals are obtained for the OLED based on the Pt(OEP) emitter. Considering that a theoretical enhancement factor of 10 is given by the NPG, as expected from our previous results [18], PEF signals of about 0.18% and 0.0017% can be estimated at a fluorophore density of $6{\cdot}10^{12}$ and $6{\cdot}10^{10}$ mol/cm^3 respectively. Such estimated PEF signals are in the same order of magnitude (or even greater) than the LSPR signal, and as well can be easily collected with standard portable electronic circuitry. Overall, an optical sensor with the optimized structure (Fig. S2) and comprising 6 sensing channels each capable of multimodal PEF and LSPR detection has been designed.

3.2. Proof-of-concept demonstration

Some experimental limitations hampered the realization of a single optical sensor with NPG, OLEDs and OPD enabling both LSPR and PEF detection modes. These limitations are related to the bio-functionalization of the NPG with fluorophore-labeled biomolecules needed for the PEF detection mode: a maximization of the coverage of the NPG surface with fluorescent-labeled targets for PEF, and an optimization of the bio-functionalization of the NPG, are first needed. In details, the concentration of fluorophores on the NPG surface which was experimentally obtained in our previous works was estimated in the order of 10 molecules/μm^2 [14]. Such amount is limited by the steric hindrance of the fluorophore, and to self-quenching effects occurring at higher concentrations. An increase of fluorophore concentration on the NPG will be considered for our future work by: i) modification of the NPG surface functionalization (e.g. by using different functional layers or 3D matrices), allowing to obtain a denser coverage of fluorophores, and/or ii) use of a different fluorophore having a lower steric hindrance and comparable or even higher quantum yield, and suitable spectral coupling with the NPG plasmonic modes. In this work, starting from the components and the layout developed in the simulations (Fig. 3a), two separated optical sensors were realized for a proof-of-concept demonstration: one optical sensor for LSPR (Fig. 3b) and one optical sensor for PEF (Fig. 3d) in a simplified version (Fig. 3e).

Table 2
Comparison between the fluorescence signals in different configurations. *PEF signal is calculated as $I_F/I_0{\cdot}10$ considering the enhancment factor reported in Ref. [18].

Configuration		Fluorescence signals			PEF signal*
Fluorophore concentration (mol/cm^3)	Emitter of the OLED for PEF	I_0 (A)	I_F (A)	I_F/I_0 (%)	$I_F/I_0 \cdot 10$ (%)
$6{\cdot}10^{10}$	$Ir(piq)_3$	$9.0{\cdot}10^{-6}$	$9.1{\cdot}10^{-13}$	$1.0{\cdot}10^{-5}$	$1.0{\cdot}10^{-4}$
	Pt(OEP)	$1.4{\cdot}10^{-7}$	$2.3{\cdot}10^{-13}$	$1.7{\cdot}10^{-4}$	$1.7{\cdot}10^{-3}$
$6{\cdot}10^{12}$	$Ir(piq)_3$	$9.0{\cdot}10^{-6}$	$9.5{\cdot}10^{-11}$	$1.1{\cdot}10^{-3}$	$1.1{\cdot}10^{-2}$
	Pt(OEP)	$1.4{\cdot}10^{-7}$	$2.5{\cdot}10^{-11}$	$1.8{\cdot}10^{-2}$	$1.8{\cdot}10^{-1}$

OLEDs and OPDs were fabricated by thermal evaporation using shadow masks. Their structure was optimized by the fine tuning of the layers' thickness and comprises a reflective Ag bottom anode electrode and a semitransparent top cathode electrode. The addition of an organic index matching layer on the top of organic stack in both the OLEDs and OPDs structures enables the maximization of the top-absorption/emission process. As the active layer of the top-adsorbing OPD, a blend of zinc phthalocyanine (ZnPc) and fullerene-C_{60} was chosen due to the wide spectral response [23] enabling detection both in the LSPR and PEF wavelength's spectral range (Fig. 4a). As light source for LSPR, OLED based on the platinum–porphyrin complex PtII–tetraphenyltetrabenzoporphyrin [Pt(tpbp)] was fabricated. According to optical simulations, the OLED based on the Pt(OEP) emitter was selected for the realization of the PEF sensor. The optoelectronic performance of the fabricated OLED are shown in Fig. 4b. In particular, the Pt(OEP) based OLED shows an optical power of 15.0 ± 3.2 μW at a current density of 31 mA/cm^2 that is reached by driving the device at 6.7 ± 0.1 V. The OLED dedicated to the LSPR detection, driven at the same density current of 31 mA/cm^2, shows an optical power of 11.8 ± 1.3 μW and a driving voltage of 6.7 ± 0.1 V. These values are comparable with similar structures reported in literature [16,24]. Fig. 4c shows the optoelectronic performance of the OPD both in dark and light condition under a simulated solar illumination (AM1.5G spectrum, optical power density 100 mW/cm^2). In particular, the realized OPDs show an open-circuit voltage (V_{OC}) of 0.5 V and a short-circuit photogenerated current density (J_{SC}) of 7.5 mA cm^{-2}, in good agreement with literature [23,25]. A responsivity (R) of 0.08 A/W and a detectivity (D*) of $1.2{\cdot}10^{11}$ Jones were calculated for the OPD under simulated solar illumination conditions, driven in reverse bias (−0.4 V), approximating the ideal shot noise with the dark current noise [26,27]. However, by providing illumination from an external light source peaked at 770 nm to mimic the emission from the OLED for LSPR, D* increases up to $1.1{\cdot}10^{12}$ Jones (data not shown), which is in line with values reported in the literature for OPDs based on ZnPc:C_{60} active layers [28]. In addition, the OPD operational regime in the sensor is 0 V. In this condition, D* is expected to increase even more. An electrically insulating and optically transparent film of a perfluorinated polymer (Cytop) was used as the spacer between OPDs and OLEDs. Fig. 4a shows the measured spectral features of the components integrated in the fabricated sensors. The optoelectronic and plasmonic components were developed in order to optically interact when integrated in the system. In particular, the emission of the OLED dedicated to PEF detection perfectly matches the absorption spectrum of the fluorophore. On the other hand, the emission of the LSPR OLED shows a good superimposition with the NPG sensitivity (calculated as the percentage variation of LSPR signal for a Δn of $2.5{\cdot}10^{-2}$ RIU). The developed OPD exhibits an external quantum efficiency (EQE) of about 20% in the spectral range compatible both with the fluorophore emission and the LSPR response, thus enabling the collection of photocurrents for the two different detection modality.

To proof experimentally the LSPR detection mode, the as-designed system (Fig. 3b) was fabricated. Fig. 3c shows the resulting optical sensor, composed of the integrated optoelectronic devices on the glass substrate, encapsulated with a transparent glass cap for better visualization, and the NPG fabricated directly onto an encapsulation glass. The

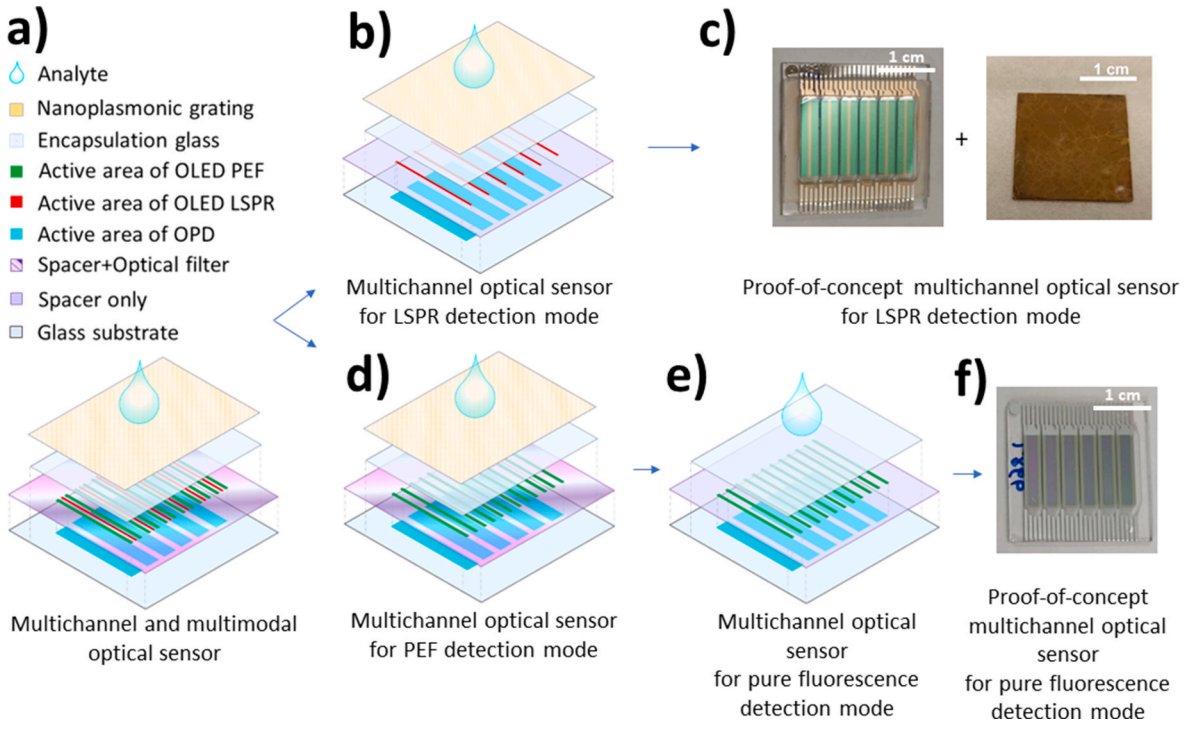

Fig. 3. (a) Schematic representation of the designed optical sensor, comprising six channels each one performing the two detection modalities LSPR and PEF. Schematic representation (b) and picture (c) of the fabricated sub-system dedicated to LSPR detection only. In (c), the picture on the left is the optoelectronic platform comprising OPDs and OLEDs for LSPR encapsulated with a transparent glass cap for better visualization, and the picture on the right is the glass cap decorated with the NPG. Schematic representation of the sub-system dedicated to PEF detection only (d). Schematic representation (e) and picture (f) of the fabricated simplified sub-system for pure fluorescence detection.

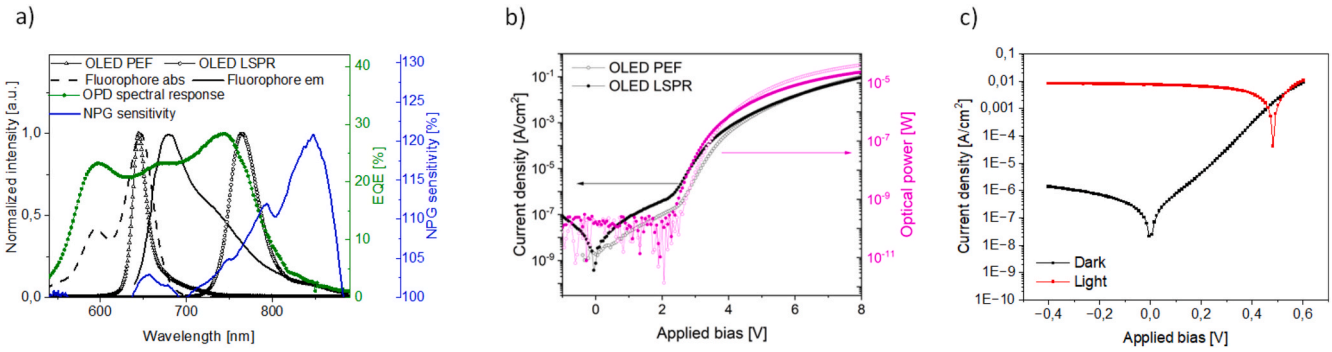

Fig. 4. a) Normalized electroluminescence spectra of the OLED for PEF (empty triangles) and OLED for LSPR (empty dots), absorption spectrum (dashed black line) and emission spectrum (solid black line) of LD700 in ethanol, spectral response (EQE) (%) of the OPD (green line), spectral sensitivity of the NPG (at normal incidence, for a Δn of $2.5{\cdot}10^{-2}$ RIU) (blue line). b) Current density (black lines) with the corresponding power of emission (pink line) for OLED dedicated to the PEF (empty dots) and LSPR detection (solid dots) fabricated on Cytop. c) Current density vs applied voltage plot (J–V plot) of the OPD measured in dark conditions (black dots) and under light illumination with an external light source (solar simulator, AM1.5G solar spectrum, optical power density 100 mW/cm^2) (red dots).

OLED for LSPR is driven at a fixed current density (31 mA/cm^2) and the OPD is driven at 0 V. The photocurrent from the OPD is collected by means of an Electrochemical Workstation over time and the NPG surface is alternately and sequentially exposed to ethanol/water solutions at different concentrations (sample solution) or water (reference solution) in the fluidic cell attached on top of the NPG. The tested refractive index changes (Δn) on the NPG surface range from $2.5{\cdot}10^{-2}$ RIU to 10^{-3} RIU. In Fig. 5a it is reported the raw photocurrent data generated over time by the OPD in the sub-system dedicated to LSPR detection. Fig. 5b shows the linear dependence between the LSPR signal ($\Delta I/I_0$) and the refractive index variation (Δn) at the NPG surface. To note, the lowest tested Δn of 10^{-3} RIU with respect to water is the value used in the simulations. At that Δn value, the experimental LSPR signal is 0.1%, with a ΔI of 1 nA over a base photocurrent I_0 of about 0.8 μA, in quite good agreement with simulations.

For the proof-of-principle of the PEF detection mode, the second sub-system needed is the PEF-dedicated optical sensor (Fig. 3d). However, further simplifications on this sub-system were needed to allow its realization and test, leading to the optical sensor sub-system reported in Fig. 3e. Such simplification is justified as follows. First, the fabrication and optimization of an optical filter with spectrally and optically matched characteristics, that could be easily implemented in the optical sensor, is challenging and it is out of the scope of this work. For this reason, the simplified optical sensor sub-system designed in Fig. 3e, and realized as reported in Fig. 3f, does not include any optical filter. Second, the experimental biofunctionalization of the NPG with Alexa Fluor 750-labeled biomolecules was optimized in our previous work [14]. Following that procedure, the resulting number of total fluorescent

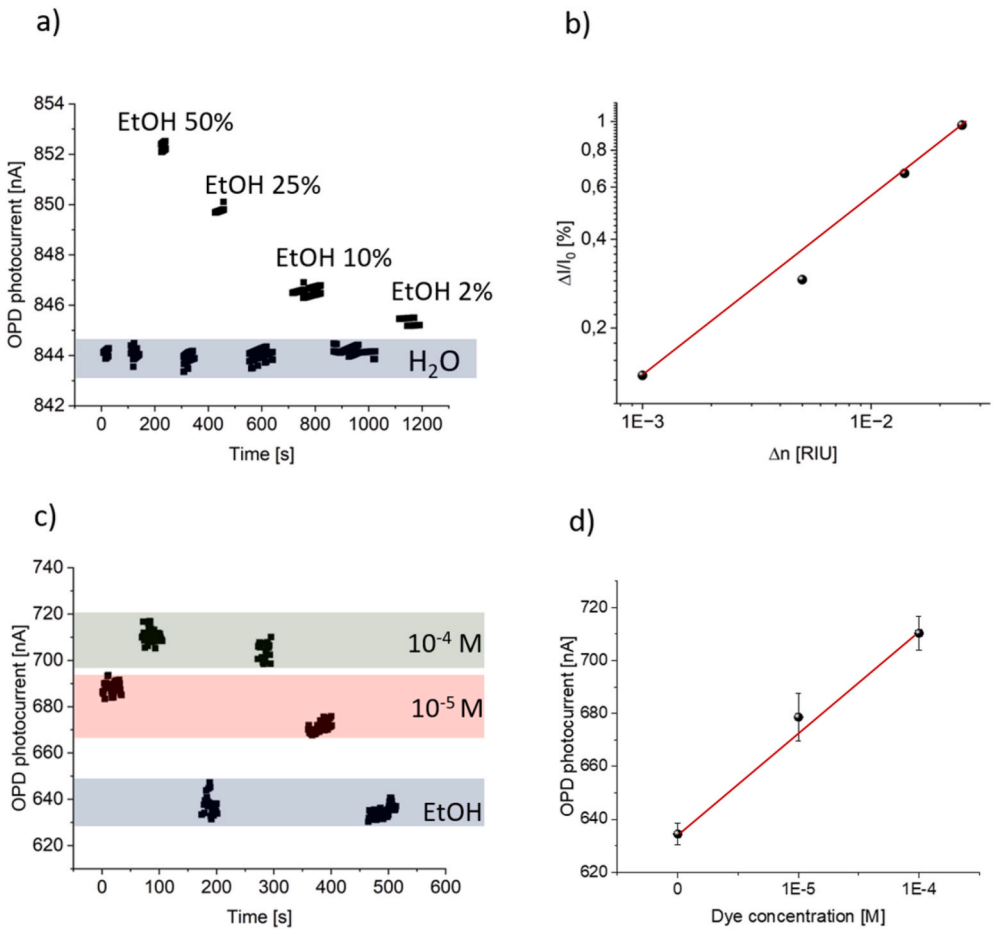

Fig. 5. LSPR and fluorescence signals collected from the dedicated optical sensors. OPD is driven at 0 V. The OLED for LSPR, driven at 31 mA/cm^2, provides illumination with a total optical power of 11.8 μW at the sensing surface. The OLED for PEF and fluorescence, driven at 31 mA/cm^2, provides illumination at a total optical power of 15.0 μW at the sensing surface. a) Experimental data of the photocurrent generated in the subsystem dedicated to the LSPR detection by the OPD over time when the NPG is exposed to ultra-pure water, 2%, 10%, 25% and 50% ethanol solutions. b) Experimental LSPR signal versus the refractive index change at the NPG surface. c) Photocurrent generated in the subsystem dedicated to the pure fluorescence detection when the sensor is exposed to pure ethanol and different LD700 solutions (10^{-4} M and 10^{-5} M). d) Experimental photocurrent from the OPD in response to different solutions: reference ethanol or LD700 solutions in ethanol.

molecules in the 10-nm thick volume above the NPG surface, at concentrations in the μM range, is extremely low. To increase the number of fluorophores while keeping the fluorophore concentration in the μM range, the optical path should be incremented, increasing the chance to achieve a measurable (pure fluorescence) signal and demonstrating as a proof-of-principle of the reliable functioning of the optical sensor. Thus, the simplified optical sensor scheme in Fig. 3e does not include the NPG.

For the fluorescence tests, Rhodamine 700 (LD700) was used as the fluorophore instead of Alexa Fluor 750. The spectral features of LD700 are still compatible with the designed sensor, as reported in Fig. 4a. In particular, the fluorophore absorption peak at around 650 nm perfectly matches the peak emission of the OLED for PEF, and the fluorescence peak at 700 nm overlaps with the spectral response of the OPD (Fig. 4a). In addition, LD700 has a higher emission quantum yield (around 0.3) with respect to Alexa Fluor 750 (around 0.1). Finally, thanks to its large use in bio-imaging and bio-diagnostics, LD700 ensures lower costs and larger availability compared to Alexa Fluor 750.

A pure ethanol solution and ethanol solutions of LD700 at a concentration of 10^{-4} M and 10^{-5} M in standard quartz cuvettes are placed sequentially on top of the optical sensor to allow measuring pure fluorescence signals. The two OLEDs for PEF are driven at a constant current density of 31 mA/cm^2 and the OPD photocurrent (OPD driven at 0 V) is recorded (see Fig. 5c). Considering that no optical filter was integrated in the sensor, the measured OPD photocurrent includes both the backscattered excitation light from the OLEDs for PEF and the pure fluorescence signal. Therefore, in Fig. 5d we simply report the total OPD photocurrent. When the sensor is exposed to pure ethanol, the recorded background photocurrent signal I_0 is about 0.6 μA (see Fig. 5c). Since no NPG is present, the light reaching the OPD is due to a non-negligible backscattered fraction of the excited light by the wall of the quartz cuvette as microfluidic system. Furthermore, it can be clearly seen that the OPD responds linearly to increasing fluorophore concentrations due to the pure fluorescence contribution, demonstrating the capability of the developed optical sensor of performing pure fluorescence detection.

These results are only a preliminary step in view of the fabrication of the multichannel and multimodal optical sensor. However, the use of the Cytop layer in the two sub-systems for LSPR and PEF, acting both as an electrical insulator/spacer between OLEDs and the underlying OPDs, and also as a protecting layer for the OPDs surface for the following fabrication steps, is a key-enabling element for the monolithic integration of the optical filter (for PEF) into the sensor. While the optical filter integration is expected not to affect the LSPR signal, as shown in the simulations, it would ensure the reduction of the background fluorescence/PEF signal and contribute to the lowering of the limit of detection in the fluorescence/PEF mode [29]. In addition, the optical sensor could benefit of the 10-times enhanced PEF signal once the NPG is integrated on top glass encapsulation lid. Considering the promising results herein reported, we aim at realizing and experimentally demonstrate the

complete, as-designed (Fig. 3a) multichannel and multimodal optical sensor in the near future.

4. Conclusions

A multichannel (enabling multiplex) and multimodal optical sensor based on organic optoelectronic and nanoplasmonic components, capable of performing LSPR and PEF detection modes, was designed and tested in proof-of-concept sub-systems. The optical sensor layout was optimized by simulations on the integrated components with matched spectral and optical characteristics. The optimized sensor comprises a NPG as the plasmonic sensing surface and multiple channels (six) working in backscattering configuration, each channel having one OPD as the light detector, one OLED enabling LSPR and two OLEDs enabling PEF, integrated onto the same 1-inch square optical sensor. The preliminary experimental results demonstrate the effectiveness of the sensor design and show a large potential for the development of a complete miniaturized optical sensor capable of multiplex and multimodal sensing.

CRediT authorship contribution statement

Emilia Benvenuti: Writing – review & editing, Writing – original draft, Investigation. **Salvatore Moschetto:** Investigation. **Marco Angelini:** Methodology, Investigation. **Franco Marabelli:** Supervision, Funding acquisition. **Marco Natali:** Investigation. **Paola Pellacani:** Writing – review & editing, Methodology, Investigation. **Margherita Bolognesi:** Writing – review & editing, Writing – original draft, Methodology, Investigation, Conceptualization. **Mario Prosa:** Writing – review & editing, Methodology, Investigation, Conceptualization. **Stefano Toffanin:** Writing – review & editing, Supervision, Funding acquisition, Conceptualization.

Declaration of competing interest

The authors declare that they have no known competing financial interests or personal relationships that could have appeared to influence the work reported in this paper.

Data availability

Data will be made available on request.

Acknowledgements

The authors thank Federico Prescimone and Vincenzo Ragona for the technical support. This work received funding from the European Union's Horizon 2020 research and innovation program under grant agreement no. 101016706 (h-ALO).

Appendix A. Supplementary data

Supplementary data to this article can be found online at https://doi.org/10.1016/j.orgel.2024.107023.

References

[1] L.F. Capitán-Vallvey, A.J. Palma, Recent developments in handheld and portable optosensing-A review, Anal. Chim. Acta 696 (2011) 27–46, https://doi.org/10.1016/j.aca.2011.04.005.
[2] R. Dragone, G. Grasso, M. Muccini, S. Toffanin, Portable bio/chemosensoristic devices: innovative systems for environmental health and food safety diagnostics, Front. Public Health 5 (2017) 1–6, https://doi.org/10.3389/fpubh.2017.00080.
[3] M. Prosa, M. Bolognesi, L. Fornasari, G. Grasso, L. Lopez-Sanchez, F. Marabelli, S. Toffanin, Nanostructured organic/hybrid materials and components in miniaturized optical and chemical sensors, Nanomaterials 10 (2020) 480, https://doi.org/10.3390/nano10030480.
[4] J.L.D. Nelis, A.S. Tsagkaris, Y. Zhao, J. Lou-Franco, P. Nolan, H. Zhou, C. Cao, K. Rafferty, J. Hajslova, C.T. Elliott, K. Campbell, The end user sensor tree: an end-user friendly sensor database, Biosens. Bioelectron. 130 (2019) 245–253, https://doi.org/10.1016/j.bios.2019.01.055.
[5] T.M. Chinowsky, J.G. Quinn, D.U. Bartholomew, R. Kaiser, J.L. Elkind, Performance of the Spreeta 2000 integrated surface plasmon resonance affinity sensor, Sens. Actuators, B 91 (2003) 266–274, https://doi.org/10.1016/S0925-4005(03)00113-8.
[6] M. Taniguchi, M.S.R. Siddiki, S. Ueda, I. Maeda, Mercury (II) sensor based on monitoring dissociation rate of the trans-acting factor MerR from cis-element by surface plasmon resonance, Biosens. Bioelectron. 67 (2015) 309–314, https://doi.org/10.1016/j.bios.2014.08.040.
[7] H. Guo, J. Li, Y. Li, D. Wu, H. Ma, Q. Wei, B. Du, A turn-on fluorescent sensor for Hg2+ detection based on graphene oxide and DNA aptamers, New J. Chem. 42 (2018) 11147–11152, https://doi.org/10.1039/c8nj01709c.
[8] J. Breault-Turcot, H.P. Poirier-Richard, M. Couture, D. Pelechacz, J.F. Masson, Single chip SPR and fluorescent ELISA assay of prostate specific antigen, Lab Chip 15 (2015) 4433–4440, https://doi.org/10.1039/c5lc01045d.
[9] Z. Lan, M.-H. Lee, F. Zhu, Recent advances in solution-processable organic photodetectors and applications in flexible electronics, Adv. Intell. Syst. 4 (2022) 2100167, https://doi.org/10.1002/aisy.202100167.
[10] S. Toffanin, V. Benfenati, A. Pistone, S. Bonetti, W. Koopman, T. Posati, A. Sagnella, M. Natali, R. Zamboni, G. Ruani, M. Muccini, N-type perylene-based organic semiconductors for functional neural interfacing, J. Mater. Chem. B 1 (2013) 3850, https://doi.org/10.1039/c3tb20555j.
[11] M. Melucci, M. Durso, C. Bettini, M. Gazzano, L. Maini, S. Toffanin, S. Cavallini, M. Cavallini, D. Gentili, V. Biondo, G. Generali, F. Gallino, R. Capelli, M. Muccini, Structure–property relationships in multifunctional thieno(bis)imide-based semiconductors with different sized and shaped N-alkyl ends, J. Mater. Chem. C 2 (2014) 3448, https://doi.org/10.1039/c3tc32538e.
[12] M. Prosa, S. Moschetto, E. Benvenuti, M. Zambianchi, M. Muccini, M. Melucci, S. Toffanin, 2,3-Thienoimide-ended oligothiophenes as ambipolar semiconductors for multifunctional single-layer light-emitting transistors, J. Mater. Chem. C 8 (2020) 15048–15066, https://doi.org/10.1039/D0TC03326J.
[13] G. Williams, C. Backhouse, H. Aziz, Integration of organic light emitting diodes and organic photodetectors for lab-on-a-chip bio-detection systems, Electronics 3 (2014) 43–75, https://doi.org/10.3390/electronics3010043.
[14] F. Lefèvre, P. Juneau, R. Izquierdo, Integration of fluorescence sensors using organic optoelectronic components for microfluidic platform, Sensor. Actuator. B Chem. 221 (2015) 1314–1320, https://doi.org/10.1016/j.snb.2015.07.077.
[15] M. Prosa, E. Benvenuti, D. Kallweit, P. Pellacani, M. Toerker, M. Bolognesi, L. Lopez-Sanchez, V. Ragona, F. Marabelli, S. Toffanin, Organic light-emitting transistors in a smart-integrated system for plasmonic-based sensing, Adv. Funct. Mater. 31 (2021) 1–12, https://doi.org/10.1002/adfm.202104927.
[16] M. Bolognesi, M. Prosa, M. Toerker, L. Lopez Sanchez, M. Wieczorek, C. Giacomelli, E. Benvenuti, P. Pellacani, A. Elferink, A. Morschhauser, L. Sola, F. Damin, M. Chiari, M. Whatton, E. Haenni, D. Kallweit, F. Marabelli, J. Peters, S. Toffanin, A fully integrated miniaturized optical biosensor for fast and multiplexing plasmonic detection of high- and low-molecular-weight analytes, Adv. Mater. 2208719 (2023), https://doi.org/10.1002/adma.202208719, 1–13.
[17] F. Floris, E. Manobianco, V. Tolardo, P. Pellacani, L. Lopez-Sanchez, F. Marabelli, Plasmonic nanostructure functionalization for surface-enhanced fluorescence bio-detection, Mater. Process. 14 (2023) 1–5, https://doi.org/10.3390/iocn2023-14524.
[18] M. Angelini, E. Manobianco, P. Pellacani, F. Floris, F. Marabelli, Plasmonic modes and fluorescence enhancement coupling mechanism: a case with a nanostructured grating, Nanomaterials 12 (2022) 1–16, https://doi.org/10.3390/nano12234339.
[19] M. Angelini, E. Manobianco, P. Pellacani, F. Floris, F. Marabelli, Refractive index dependence of fluorescence enhancement in a nanostructured plasmonic grating, Materials 16 (2023), https://doi.org/10.3390/ma16031289.
[20] J.L. Ballard, V.K. Peeva, C.J.S. DeSilva, J.L. Lynch, N.R. Swanson, Comparison of Alexa Fluor® and CyDye™ for practical DNA microarray use, Mol. Biotechnol. 36 (2007) 175–183, https://doi.org/10.1007/s12033-007-0006-4.
[21] A. Tsuboyama, H. Iwawaki, M. Furugori, T. Mukaide, J. Kamatani, S. Igawa, T. Moriyama, S. Miura, T. Takiguchi, S. Okada, M. Hoshino, K. Ueno, Homoleptic cyclometalated iridium complexes with highly efficient red phosphorescence and application to organic light-emitting diode, J. Am. Chem. Soc. 125 (2003) 12971–12979, https://doi.org/10.1021/ja034732d.
[22] D. Li, L.S. Liao, Highly efficient deep-red organic light-emitting diodes using exciplex-forming co-hosts and thermally activated delayed fluorescence sensitizers with extended lifetime, J. Mater. Chem. C 7 (2019) 9531–9536, https://doi.org/10.1039/c9tc02834j.
[23] S. Döring, T. Otto, M. Cehovski, O. Charfi, R. Caspary, W. Kowalsky, T. Rabe, Highly sensitive wide range organic photodiode based on zinc phthalocyanine:C 60, Phys. Status Solidi 213 (2016) 2387–2391, https://doi.org/10.1002/pssa.201532856.
[24] R.C. Kwong, S. Sibley, T. Dubovoy, M. Baldo, S.R. Forrest, M.E. Thompson, Efficient, saturated red organic light emitting devices based on phosphorescent platinum(II) porphyrins, Chem. Mater. 11 (1999) 3709–3713, https://doi.org/10.1021/cm9906248.
[25] W. Tress, A. Merten, M. Furno, M. Hein, K. Leo, M. Riede, Correlation of absorption profile and fill factor in organic solar cells: the role of mobility imbalance, Adv. Energy Mater. 3 (2013) 631–638, https://doi.org/10.1002/aenm.201200835.
[26] C. Fuentes-Hernandez, C. Fuentes-Hernandez, W.-F. Chou, T.M. Khan, L. Diniz, J. Lukens, F.A. Larrain, V.A. Rodriguez-Toro, B. Kippelen, Large-area low-noise

flexible organic photodiodes fordetecting faint visible light, Science 370 (2020) 698–701. https://www.science.org/doi/10.1126/science.aba2624.
[27] G. Liu, T. Li, X. Zhan, H. Wu, Y. Cao, High-sensitivity visible–near infrared organic photodetectors based on non-fullerene acceptors, ACS Appl. Mater. Interfaces 12 (2020) 17769–17775, https://doi.org/10.1021/acsami.0c00191.
[28] J. Kublitski, A. Hofacker, B.K. Boroujeni, J. Benduhn, V.C. Nikolis, C. Kaiser, D. Spoltore, H. Kleemann, A. Fischer, F. Ellinger, K. Vandewal, K. Leo, Reverse dark current in organic photodetectors and the major role of traps as source of noise, Nat. Commun. 12 (2021) 551, https://doi.org/10.1038/s41467-020-20856-z.
[29] E. Benvenuti, A. Lanfranchi, S. Moschetto, M. Natali, M. Angelini, P. Lova, F. Prescimone, V. Ragona, D. Comoretto, M. Prosa, M. Bolognesi, S. Toffanin, On-chip organic optoelectronic system for fluorescence detection, J. Mater. Chem. C (2024), https://doi.org/10.1039/D3TC04321E. Advance Article.